Journal of Alloys and Compounds 1007 (2024) 176453

Contents lists available at ScienceDirect

Journal of Alloys and Compounds

journal homepage: www.elsevier.com/locate/jalcom

Fine-grained BCZT piezoelectric ceramics by combining high-energy mechanochemical synthesis and hot-press sintering

M.J. Sayagués [a], A. Otero [b], L. Santiago-Andrades [a], R. Poyato [a], M. Monzón [c], R. Paz [c], F.J. Gotor [a], R. Moriche [b,*]

[a] Instituto de Ciencia de Materiales de Sevilla (ICMS), CSIC-US, Américo Vespucio, 49, Sevilla 41092, Spain
[b] Departamento de Física de la Materia Condensada, Facultad de Física, Universidad de Sevilla-ICMS, Avda. Reina Mercedes, s/n, Sevilla 41012, Spain
[c] Departamento de Ingeniería Mecánica, Grupo de Investigación en Fabricación Integrada y Avanzada, Universidad de Las Palmas de Gran Canaria, Campus Universitario de Tafira s/n, Las Palmas 35017, Spain

ARTICLE INFO

Keywords:
Lead-free piezoceramics
BCZT
Mechanosynthesis
Piezoelectric properties
Dielectric properties

ABSTRACT

Different stoichiometries of lead-free $BaZr_{0.2}Ti_{0.8}O_3$–$Ba_{0.7}Ca_{0.3}TiO_3$ (BCZT) prepared by mechanosynthesis and sintered by either conventional sintering (CS) or hot pressing (HP) techniques were studied to establish the dependence of piezoelectric and dielectric properties on sintering parameters and microstructure. All synthesized stoichiometries showed a pseudocubic perovskite phase with homogeneously distributed A- and B-cations in the structure. The BCZT retained the pseudocubic symmetry after sintering and an average grain size <1.8 μm was obtained in all cases. HP sintering hindered the secondary phase segregation observed in the CS ceramics and increased the relative density. Piezoelectric coefficients (d_{33}) ranging from 5.1 to 21 pC/N and from 10.0 to 88.0 pC/N were obtained for CS and HP ceramics, respectively, despite the pseudocubic symmetry and the fine grain size. The higher d_{33} values for the HP ceramics are a consequence of the higher density, better chemical homogeneity and lower sintering temperature and time required for the mechanosynthesized BCZT powders with high sintering activity.

1. Introduction

To date, lead zirconate titanate (PZT) has been one of the main piezoceramics used in actuators and other electromechanical devices due to its high piezoelectric (d_{33}) and electromechanical coupling (k_{33}) coefficients, which are in the range of 200–600 pC/N and 0.6–0.8, respectively [1]. However, the high toxicity of lead is a limitation due to growing environmental concerns worldwide. Therefore, the search for alternative environmentally friendly materials that retain the properties required for technological applications is one of the hot topics in materials science.

In 2009, Liu and Ren [2] proposed the BTZ-BCT (or BCZT) system ($Ba(Ti_{0.8}Zr_{0.2})O_3$-$(Ba_{0.7}Ca_{0.3})TiO_3$) with $d_{33} \sim 620$ pC/N at optimal composition as a real lead-free alternative to PZT [3–6] and it was highlighted the importance of searching for systems with morphotropic phase boundaries (MPB) [7,8]. In the case of the BCZT system, the high piezoelectricity comes from the existence of a cubic-rhombohedral-tetragonal (C-R-T) triple point in the phase diagram that induces a very low energy barrier for polarization rotation and lattice distortion in compositions close to the MPB region, where dissimilar ferroelectric domains coexist [9,10]. Consequently, stoichiometry plays a key role in maximizing the piezoelectric response of these ceramics [11].

In addition, the microstructure of sintered BCZT is also of great importance. Fine-grained ceramics are interesting because mechanical properties can be improved, but for BCZT piezoceramics, the grain size effect is an issue as smaller grains lead to a reduction in piezoelectric properties [4–6]. In studies regarding $(Ba_{0.85}Ca_{0.15})(Zr_{0.10}Ti_{0.90})O_3$ ceramics, Hao et al. [12] reported a decrease in d_{33} from ~470 to ~72 pC/N for grain sizes from 10 to 0.4 μm, and Coondoo et al. [4] reported a decrease from 345 to 39 pC/N for grain sizes of 27 and 1.5 μm. In the study by Yan et al. [5], $0.4Ba(Zr_{0.2}Ti_{0.8})O_3$-$0.6(Ba_{0.7}Ca_{0.3})TiO_3$ ceramics with grain sizes ranging from 2 to 24 μm were studied and a critical grain size of ~ 12.9 μm was identified, as significant decreases in permittivity and d_{33} piezoelectric coefficient were observed in ceramics with smaller grain sizes.

On the other hand, BCZT ceramics may exhibit abnormal grain growth with grain sizes typically larger than 10 μm [4,13–15] with

* Corresponding author.
E-mail address: rmoriche@us.es (R. Moriche).

https://doi.org/10.1016/j.jallcom.2024.176453
Received 22 June 2024; Received in revised form 27 August 2024; Accepted 9 September 2024
Available online 10 September 2024

Table 1
Stoichiometry and nomenclature of the BCZT samples obtained by mechanochemistry, annealed at 900 ºC and further sintered by conventional method (CS) and hot press (HP) for the different x values in the system (1-x)$BaZr_{0.2}Ti_{0.8}O_3$–(x)$Ba_{0.7}Ca_{0.3}TiO_3$.

x	Stoichiometry	Milled samples	Annealed samples	CS samples	HP samples
0.4	$\mathbf{Ba_{0.88}Ca_{0.12}Zr_{0.12}Ti_{0.88}O_3}$	**BCZT−04**	**900-BCZT−04**	**CS-BCZT−04**	**HP-BCZT−04**
0.45	$\mathbf{Ba_{0.865}Ca_{0.135}Zr_{0.11}Ti_{0.89}O_3}$	**BCZT−045**	**900-BCZT−045**	**CS-BCZT−045**	**HP-BCZT−045**
0.5	$\mathbf{Ba_{0.85}Ca_{0.15}Zr_{0.1}Ti_{0.9}O_3}$	**BCZT−05**	**900-BCZT−05**	**CS-BCZT−05**	**HP-BCZT−05**
0.55	$\mathbf{Ba_{0.835}Ca_{0.165}Zr_{0.09}Ti_{0.91}O_3}$	**BCZT−055**	**900-BCZT−055**	**CS-BCZT−055**	**HP-BCZT−055**
0.6	$\mathbf{Ba_{0.82}Ca_{0.18}Zr_{0.08}Ti_{0.92}O_3}$	**BCZT−06**	**900-BCZT−06**	**CS-BCZT−06**	**HP-BCZT−06**

inhomogeneous microstructures because of the high sintering temperatures usually required to densify the ceramic powders obtained by conventional routes, such as the solid-state method [4,14,15]. This could hinder their application in microelectronics, where it is essential that the ceramics have dense, homogeneous, and fine-grained microstructures to maintain mechanical strength and improve reliability. Thus, considerable efforts are being made in several research groups to achieve a microstructural refinement in BCZT while avoiding a significant degradation of the piezoelectric performance.

The use of non-conventional sintering techniques, such as Spark Plasma Sintering (SPS) [12,13,16] or Flash Sintering (FS) [17], has been proposed to refine the BCZT ceramic microstructure. In the study by Hao et al. [12], spark plasma sintering of powders obtained by the solid-state method resulted in submicrometric grain sizes of ~ 0.4 μm for $(Ba_{0.85}Ca_{0.15})(Zr_{0.10}Ti_{0.90})O_3$ ceramics with a d_{33} of 72 pC/N. Recent studies have combined these non-conventional sintering techniques with a high-energy powder mechanosynthesis route. In the study by López-Blanco et al. [17] d_{33} of 100–145 pC/N were obtained for flash-sintered $(Ba_{0.85}Ca_{0.15})(Zr_{0.10}Ti_{0.90})O_3$ ceramics with grain sizes of ~ 2 μm, however, lower d_{33} values, between 17 and 45 pC/N, were reported for spark plasma sintered ceramics of the same composition with smaller grain sizes (~ 1–2 μm) [16].

Nevertheless, conventional sintering techniques may be simpler, more scalable, and cost-effective than SPS or FS, and when combined with powder processing routes that provide highly reactive powders, such as sol-gel or mechanosynthesis, could also provide fine-grained BCZT ceramics. For example, in the study by Yan et al. [5], the application of a two-step sintering method to powders synthesized by a combination of the conventional solid-state reaction and high-energy milling resulted in ceramics with a grain size of 2 μm that maintained a d_{33} value of 120 pC/N. However, in the study by Coondoo et al. [4], conventional sintering of highly reactive powders synthesized by sol-gel resulted in ceramics with a grain size of 1.5 μm, but a decrease in the d_{33} coefficient to 39 pC/N was reported. In any case, the strong dependence of the piezoelectric properties of BCZT ceramics on the composition, structure, and microstructure, which in turn are highly dependent on the synthesis and sintering methods employed, means that a wide range of d_{33} values for this system can be found in the literature.

In this study, (1-x)$BaZr_{0.2}Ti_{0.8}O_3$–(x)$Ba_{0.7}Ca_{0.3}TiO_3$ powder phases with different stoichiometries selected within the MPB region were obtained by mechanosynthesis. The mechanochemical process is an energy and time efficient and convenient method for the preparation of BCZT compared to thermal based methods. In addition, it is a dry and solvent-free process and therefore has the advantage over other more complicated solution-based processes, such as Pechini and sol-gel methods, of producing no waste during preparation, which is an additional benefit from an environmental point of view. Mechanochemistry is characterized by its relative simplicity, scalability and minimal use of expensive materials. The ceramic powders were then consolidated by conventional sintering in a furnace at 1450 ºC/4 h or by hot pressing at 1400 °C/1 h and 30 MPa, after thermal treatment at 900 ºC/1 h. The crystal structure was determined by X-ray diffraction using Rietveld refinement, and the microstructural features were analyzed by scanning and transmission electron microscopy. The dependence of piezoelectric and dielectric properties on sintering parameters and microstructure was studied.

2. Materials and Methods

A set of samples belonging to the system (1-x)$BaZr_{0.2}Ti_{0.8}O_3$–(x)$Ba_{0.7}Ca_{0.3}TiO_3$ (BCZT) with x = 0.4, 0.45, 0.5, 0.55 and 0.6 were synthesized by mechanochemistry in a high-energy planetary mill (Micro Mill Pulverisette 7, Fritsch). Stoichiometric mixtures of barium peroxide (BaO_2, CAS Number 1304–29–6, Aldrich, 95 % in purity); calcium oxide obtained from calcination at 1000 ºC/3 h of calcium carbonate ($CaCO_3$, CAS Number 471–341, Aldrich, 98 % in purity); zirconium (IV) oxide (ZrO_2, CAS Number 1314–23–4, Aldrich, 99 % in purity) and titanium (IV) oxide (TiO_2, CAS Number 13463–677, Aldrich, 99.5 % in purity). Although $BaCO_3$ and $CaCO_3$ are commonly used in powder synthesis from thermal processes, they cannot be used directly as reagents in mechanochemical processes because their decomposition and removal of CO_2 cannot be induced during milling, even under high energy conditions. It is possible to use BaO_2 as a Ba precursor, but there is no similar commercial product of sufficient chemical quality for Ca, so it was necessary to thermally decompose $CaCO_3$ prior to milling and use it quickly to carry out the mechanochemical synthesis to avoid hydration and carbonation.

The stoichiometric mixtures of reactant powders to obtain 5 g of each sample were placed in a 60 mL tempered steel vial (inner diameter = 45 mm) together with six tungsten carbide (WC) balls (Ø = 15 mm and m = 26.4 g, ball-to-powder ratio (BPR) equal to 28) and subjected to a rotational speed of the supporting disk of 600 rpm for 120 min. The milling time was previously optimized by stopping the process at increasing intervals (every 15–30 min) and inspecting the product by X-ray diffraction (XRD) until full conversion of the designed samples was achieved. To avoid contamination of the obtained powders with the milling media (Fe or WC), a first sample batch was prepared and discarded, so that for the following batches the walls of the jar and the balls were protected with the composition system. Subsequently, the powder samples obtained by mechanosynthesis were thermally treated at 900 ºC/1 h in order to homogenize the powder prior to the sintering treatment. The nomenclature and stoichiometry of each sample are presented in Table 1.

The powder of each sample was conformed into a 15 mm disc and pressed at 15 ton for 10 min using a uniaxial press and densified using two different sintering methods. A conventional sintering (CS) by thermal treatment at high temperature (1450 ºC/4 h) in atmospheric air (heating and cooling rates of 5 ºC/min) in a tubular furnace, and a hot-press sintering (HP) at 1400 ºC/1 h in vacuum at a pressure of 30 MP (heating and cooling rates of 6 and 10 ºC/min, respectively) in a Termolab HP2500 equipment. The bulk density of the sintered ceramics was measured by the Archimedes method using distilled water and the relative density was calculated from the theoretical density values.

Phase analysis and crystal structure were analyzed from XRD patterns collected using Cu $K\alpha$ radiation on an X'Pert Pro MPD instrument (PANalytical) equipped with a θ/θ goniometer, a graphite-diffracted beam monochromator and a solid-state detector (X'Cellerator). The diffraction patterns were scanned from 10 to 120° (2θ) in step-scan mode with a step size of 0.017° and a counting time equivalent to 500 s/step. The diffraction line positions were corrected with silicon powder (Standard Reference Material 640c, NIST). The X'Pert HighScore Plus software (version 3.0.5, PANalytical) was used for line profile,

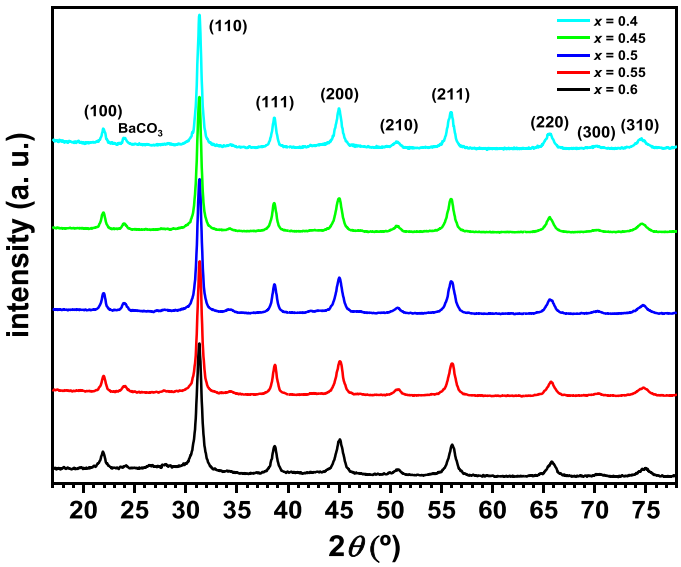

Fig. 1. XRD patterns of the different $BaO_2/CaO/ZrO_2/TiO_2$ powder mixtures after 120 min of milling where the formation of a perovskite phase with cubic symmetry is observed.

crystallographic and Rietveld refinement analysis.

The morphology of the sintered samples was analyzed by scanning electron microscopy (SEM) on fracture surfaces after thermal revealing at 150 °C below the sintering temperature for 20 min. To prevent electrical charge, the samples were coated with a gold layer. Secondary and retro-dispersed electron images were obtained on an S-4800 field emission gun (FEG) microscope (Hitachi, Japan) at an accelerating voltage of 2 kV. Chemical homogeneity was confirmed through energy dispersive X-ray spectroscopy (EDS) by means of a Bruker detector coupled to the SEM microscope using an acceleration voltage of 20 kV. Chemical mappings and semiquantitative analysis were performed in multiple areas of the samples. The planar grain size was estimated as the equivalent planar diameter, $d = 2(area/\pi)^{1/2}$. At least, 100 grains were measured to obtain the average value.

Microstructural characterization of sintered discs was also performed using transmission electron microscopy (TEM) and related techniques. Two different equipment were used: TECNAI FEG microscope (model G2 F30 S- twin, FEI Company) (0.2 nm point resolution) working at 300 kV with scanning-transmission capabilities (STEM) and TALOS™ F200S G2 S/TEM scanning/transmission electron microscope (STEM) Remote Control (FEI High-resolution), working at 200 kV and equipped with a high-angle annular dark-field (HAADF) detector, a high stability FEG emitter (point resolution 0.25 nm), an analytical objective lens with constant power and automated objective aperture and a Super-X 2SDD EDX system that includes two silicon drift detectors. The elemental mapping experiments were performed by combining HAADF and EDS acquisitions in STEM mode and were accomplished with the VELOX software (FEI Europe). HR micrograph analysis, lattice parameters, interplanar spacing, fast Fourier transform (FFT) and phase interpretation were done with the Gatan Digital micrograph software (Gatan Inc.) and the Java version of the Electron Microscope Software (JEM, Japan).

Poling of sintered ceramics was carried out in a silicon oil bath at 100 °C under a DC electric field of 4 kV/mm for 30 min using a high voltage power supply (+30 kV/2 mA) supplied by *PolyK* (PA, USA). The electric field was maintained until the sample reached 30 °C. The piezoelectric coefficient (d_{33}) was measured in a Berlincourt piezo d_{33} meter equipped with a static force sensor from *PolyK* (PA, USA). The permittivity was measured at room temperature before poling using an SES Instrument Model DEC-01 (SES Instruments Pvt Ltd, Roorkee, India).

Table 2
Lattice parameter of the BCZT perovskite phase obtained by mechanochemistry, annealed at 900 °C and further sintered by conventional method (CS) and hot press (HP) for the different x values in the system $(1-x)BaZr_{0.2}Ti_{0.8}O_3$–$(x)Ba_{0.7}Ca_{0.3}TiO_3$ assuming a pseudocubic crystal structure.

x	Lattice parameters, Å			
	Milled samples	**Annealed samples**	**CS samples**	**HP samples**
0.4	4.025(1)	4.0235(4)	4.0274(1)	4.0250(1)
0.45	4.023(1)	4.0186(6)	4.0193(1)	4.0210(1)
0.5	4.020(1)	4.0159(4)	4.0241(1)	4.0192(1)
0.55	4.014(1)	4.0107(5)	4.0073(1)	4.0111(1)
0.6	4.011(2)	4.0053(6)	4.0069(1)	4.0062(1)

3. Results and discussion

Fig. 1 shows the XRD patterns of the samples obtained by milling the different stoichiometric reactant mixtures under the experimental conditions described above. The patterns indicate the presence of a perovskite phase in all samples, suggesting the formation of the solid solution in the BCZT system with homogeneously distributed A- and B-cations in the crystal structure. In addition, a small amount of $BaCO_3$ was observed, which was already present as a secondary phase in the BaO_2 reactant. It is important to note that the high-energy mechanochemical process used in this study allowed the BCZT perovskite phase to be obtained in a shorter time compared to previous works [6,17,18]. Note that BaO_2 is a highly reactive compound and favors the mechanochemical process. In addition, oxygen is released during the mechanochemical reaction, so the milling process is performed in an oxygen-rich, over-pressurized, closed atmosphere.

Furthermore, the significant broadening of the XRD diffraction peaks in Fig. 1, which indicates the presence of small crystalline domains and a high density of defects due to the high energy intensity milling regime, did not allow resolving the actual crystal structure of the perovskite phase, and a cubic or pseudocubic phase (space group *Pm-3 m*) was observed. The corresponding (h k l) planes are marked in Fig. 1. Previous studies have reported similar observations when synthesizing other perovskite materials under comparable mechanochemical conditions, and the true structure was resolved only after thermal treatment at high temperature [19–22]. The lattice parameters for the different BCZT samples were calculated and similar values were obtained as shown in Table 2. Only a slight decrease in the cell parameter was observed with increasing x value (corresponding to decreasing and increasing contents of Zr and Ca, respectively). Coherent diffraction domains of approximately 18 nm were determined from the full-width at half-maximum (FWHM) values of the diffraction peaks.

After annealing at 900 °C, the $BaCO_3$ impurity phase disappeared (all Ba was incorporated into the solid solution) and the broadening of the XRD diffraction peaks was slightly reduced (diffraction domains of about 25 nm), but the pseudocubic crystal structure was retained. The XRD patterns in Fig. 2 are consistent with a perovskite BCZT single phase with any other secondary phase. The lattice parameters of the annealed BCZT samples (Table 2) exhibited the same trend of slight decrease with increasing x value, as evidenced by the shift of the XRD peaks to higher angles, which is more clearly observed by enlarging the 30–33° (2θ) region of the (110) peak (Fig. 2). As mentioned above, as the x value increases, the amount of Zr^{4+} (ionic radius = 0.72 pm) replacing Ti^{4+} (ionic radius = 0.605 pm) in octahedral coordination decreases, while the amount of Ca^{2+} (ionic radius = 1.34 pm) replacing Ba^{2+} (ionic radius = 1.61 pm) in 12-fold coordination increases. Therefore, both substitutions in the A- and B-positions of the perovskite structure are consistent with a smaller cell volume at higher x values and confirm the formation of the BCZT solid-solution.

The XRD patterns of the ceramic samples after conventional and hot-press sintering are shown in Figs. 3 and 4, respectively, where the BCZT phase with perovskite structure is observed. However, samples **CS-**

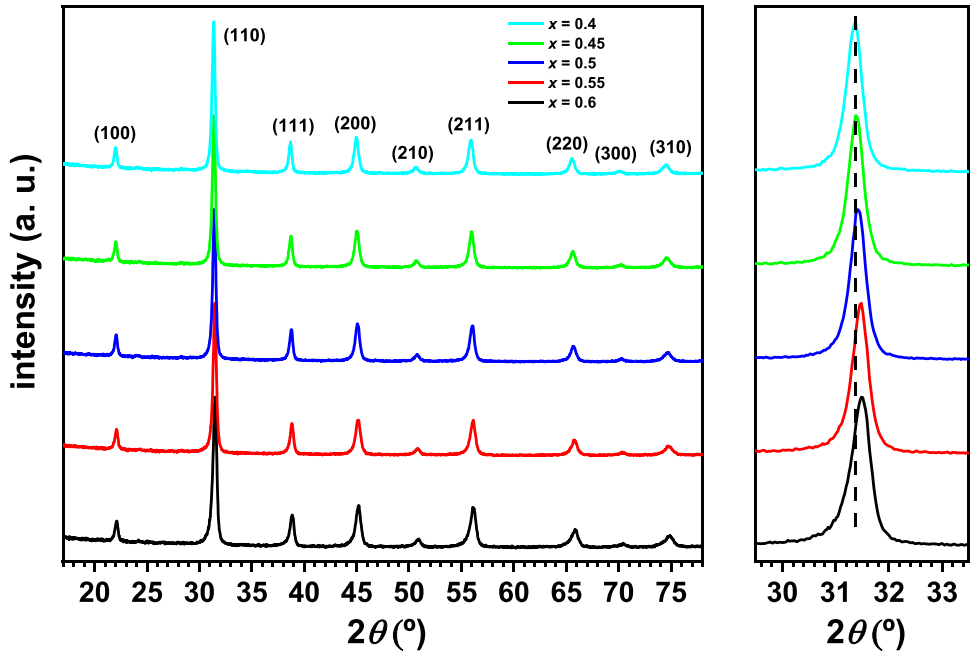

Fig. 2. XRD patterns of the different BCZT samples obtained by mechanochemistry after the annealing at 900 ºC.

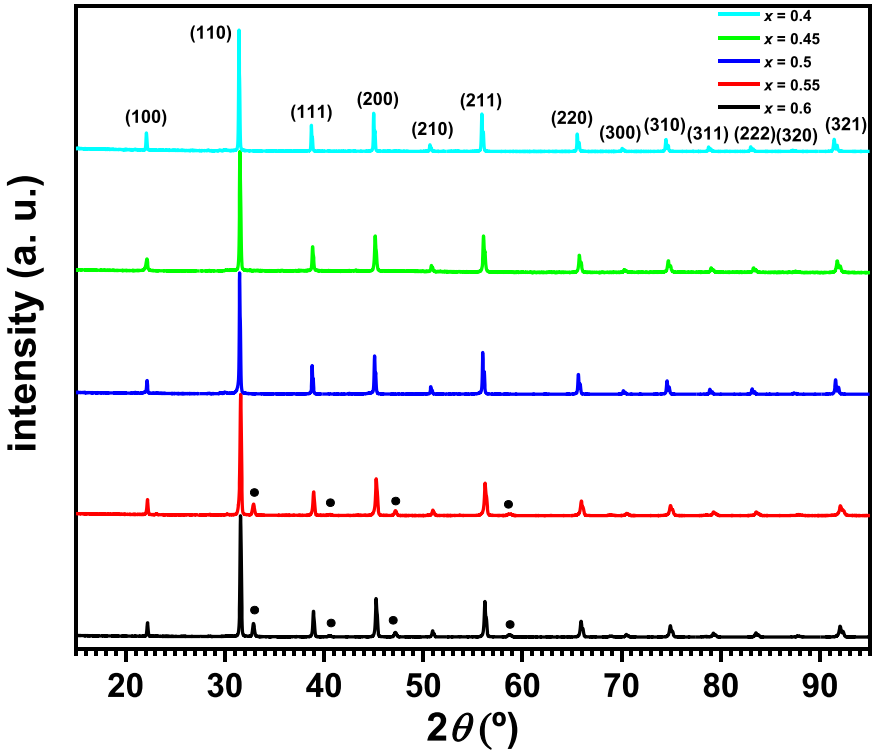

Fig. 3. XRD patterns of the different BCZT ceramic samples densified by conventional sintering. (•) Secondary phase with $A_4B_3O_{10}$ crystal structure.

BCZT-06 and **CS-BCZT-055** show the presence of a non-negligible amount of a secondary phase with chemical formula $A_4B_3O_{10}$ and Ruddlesden-Popper structure with n=3 ($A_{n+1}B_nO_{3n+1}$, where $n$$ABO_3$ perovskite and 1-AO rock salt layers alternately are stacked along the c-axis). Phase quantification by Rietveld refinement revealed an $A_4B_3O_{10}$ content of ~ 23.5 and 20.5 % for **CS-BCZT-06** and **CS-BCZT-055**, respectively. The same secondary phase was also observed in **HP-BCZT-045**, but to a lesser extent (~ 6.0 %). Although not observed in Figs. 3 and 4 due to the y-axis intensity, a secondary phase with A_2BO_4 formula and Ruddlesden-Popper structure with n=1 was also detected in **CS-BCZT-05**, **HP-BCZT-06**, **HP-BCZT-055** and **HP-BCZT-04** samples, but always in a minor proportion (< 3 %). These secondary phases, mainly observed in BCZT samples with higher Ca content, may be formed due to the high-temperature treatment and the presence of local chemical inhomogeneities. It is clear that hot-press sintering better prevents possible secondary phase segregation during processing in the mechanochemically synthesized powders.

It is known that BCZT samples with chemical compositions similar to

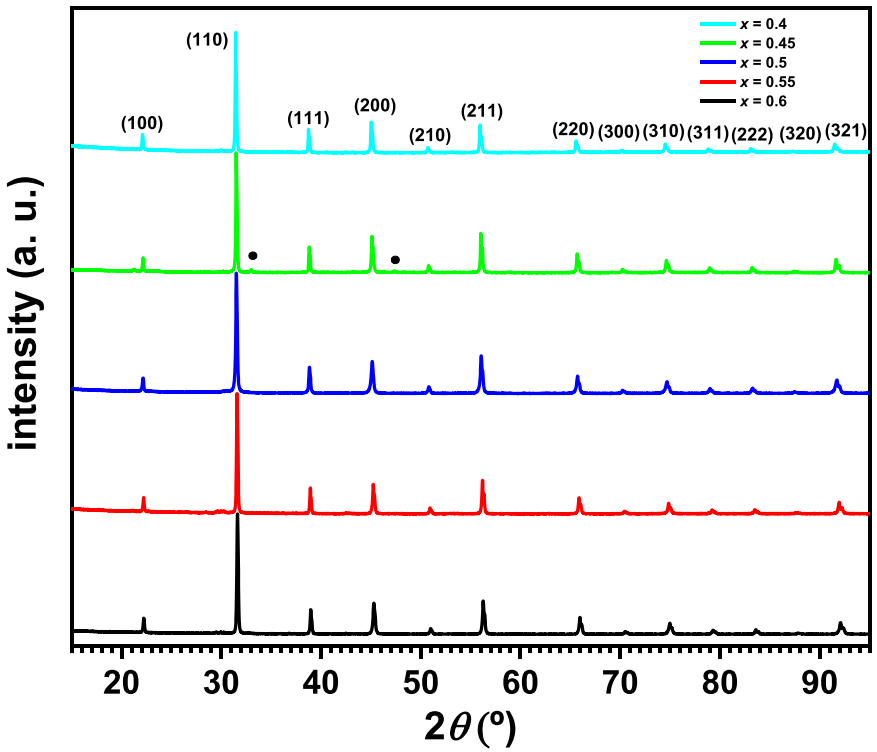

Fig. 4. XRD patterns of the different BCZT ceramic samples densified by hot-press sintering. (●) Secondary phase with $A_4B_3O_{10}$ crystal structure.

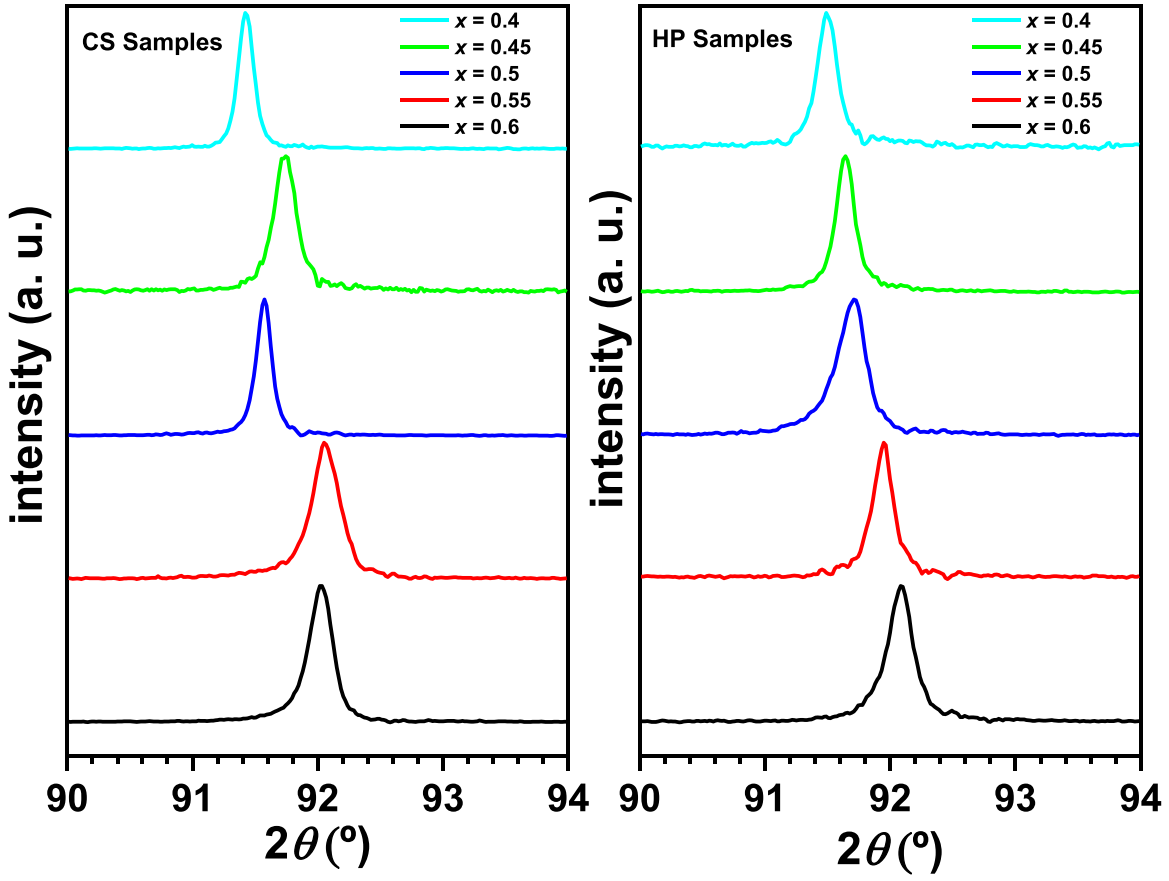

Fig. 5. XRD patterns of the different BCZT sintered samples in the 90–94º (2θ) region corresponding to the (321) diffraction line with pseudocubic symmetry. The $K\alpha_2$ peak was stripped.

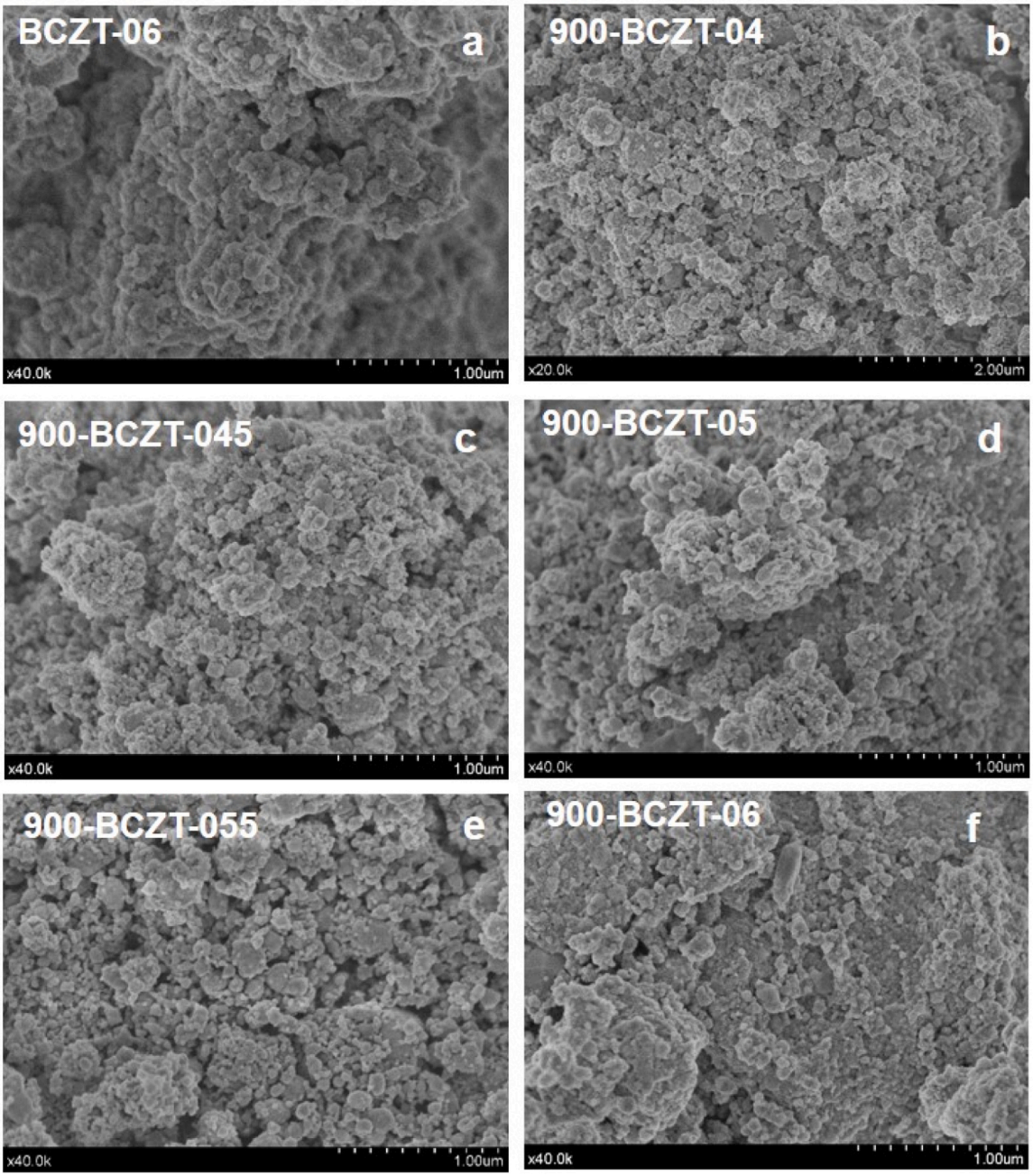

Fig. 6. (a) SEM micrograph of the **BCZT-06** milling powder and (b-f) SEM images from all BCZT samples after treatment at 900 ºC/*1 h*.

those studied in this work are in the MPB region, and the presence of orthorhombic, tetragonal and even rhombohedral phases at room temperature has been frequently reported [7,23,24]. However, the BCZT perovskite phases shown in Figs. 3 and 4 exhibit a crystal structure more compatible with pseudocubic symmetry after sintering. XRD peak splitting was not observed in these patterns, even in the high-angle region, probably indicating the presence of misoriented crystal domains with small local structural distortions leading to global pseudocubic symmetry. For example, in the region of the (321) diffraction line for pseudocubic symmetry (90–94º (2θ) range), a multiplet XRD peak is expected in a rhombohedral, orthorhombic or tetragonal structure. However, in Fig. 5, which shows the XRD pattern in this region (with the $K\alpha_2$ peak stripped for clarity), a unique and nearly symmetrical peak is observed for both sintered sample sets. Furthermore, the broadening of this diffraction line is not large enough to conclude unequivocally that it was formed by multiple peaks. Moreover, for the HP samples (Fig. 5), a continuous shift of the XRD peak position as a result of the different chemical composition of the BCZT solid solution was observed. However, for the CS samples, this shift was not so straightforward due to the presence of the secondary phases mentioned above, which modified the final chemical composition of the BCZT solid solution.

Although examples can be found in the literature where XRD patterns such as those shown in Figs. 3 and 4 are analyzed assuming a mixture of phases corresponding to the MPB region, the truth is that good Rietveld refinements can be obtained assuming the presence of a single phase or different mixtures of them with slight differences in lattice parameters and contents, and the choice of the correct solution cannot be reached in an unambiguous way without further characterizations and evidence. For all these reasons, it was considered more convenient to index the XRD patterns in Figs. 3 and 4 assuming a pseudocubic structure, and the lattice parameters obtained are presented in Table 2. Several studies have already shown that BCZT ceramic

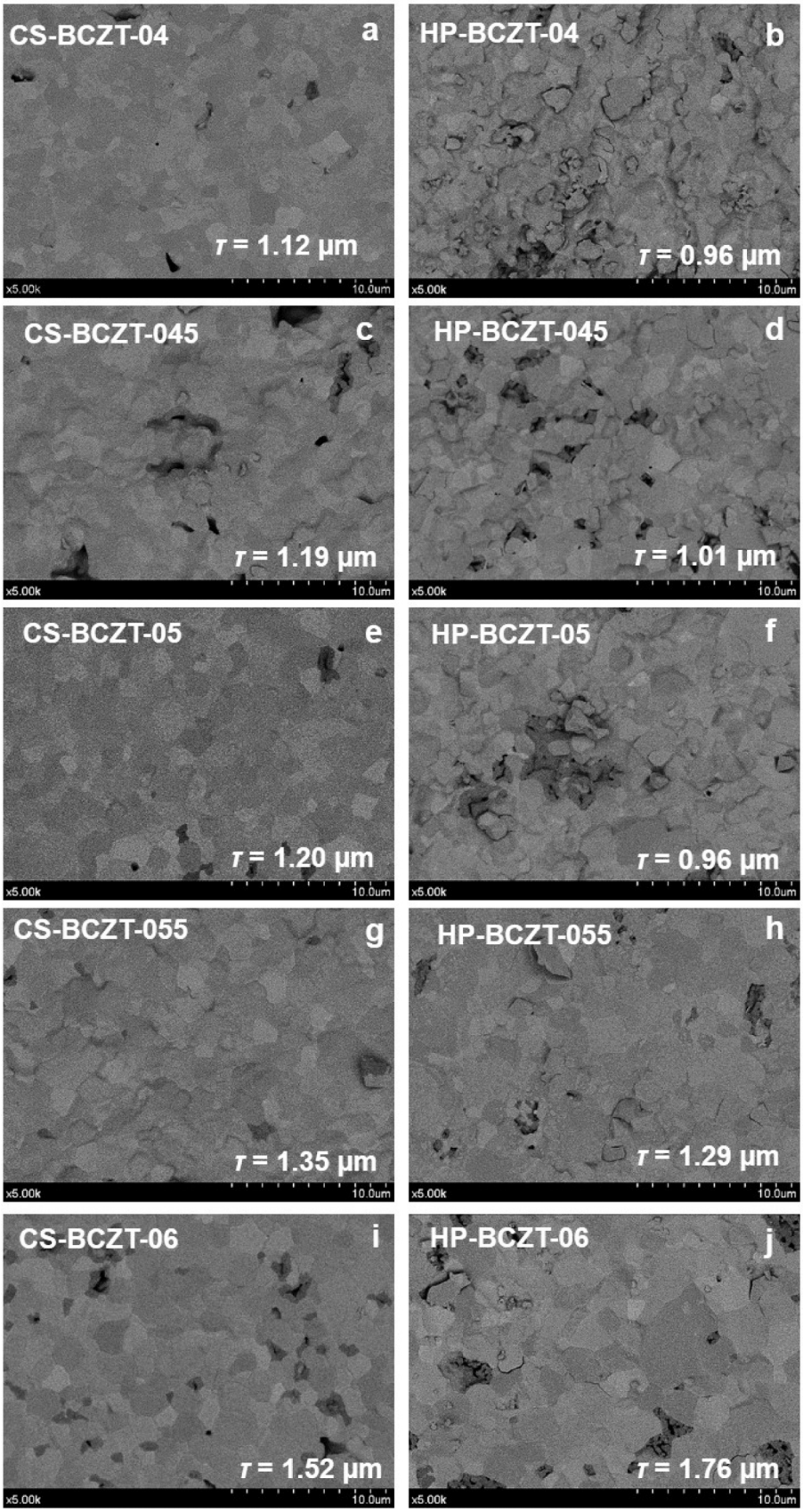

Fig. 7. BS-SEM images of the conventional (CS) and hot press (HP) sintered BCZT samples; the average grain size is inset in each image.

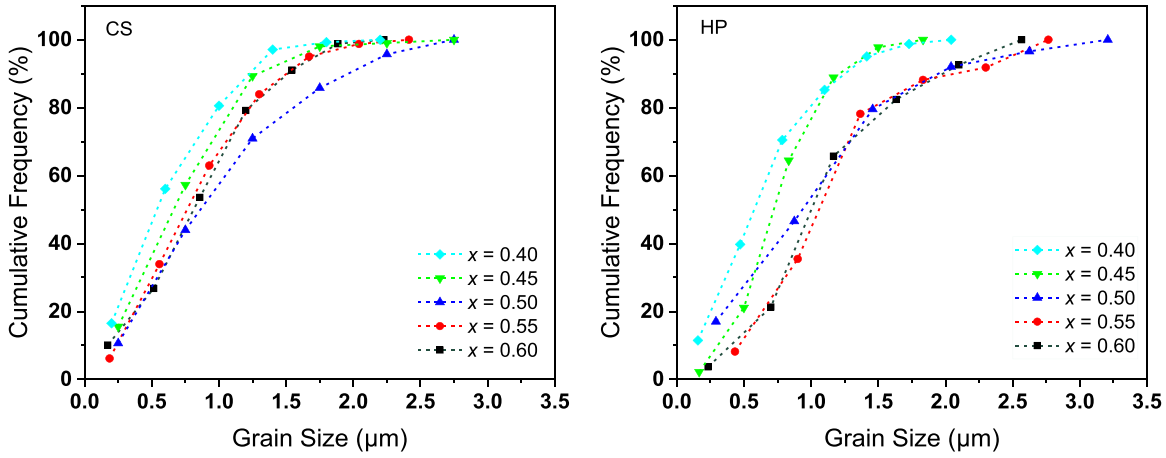

Fig. 8. Cumulative frequency versus grain size of the conventional (CS) and hot press (HP) sintered BCZT samples obtained from the SEM images.

samples with fine-grained microstructure exhibit pseudocubic symmetry by XRD while retaining ferroelectric character [4,13,17].

The mechanochemically synthesized powders were analyzed by SEM technique, and a microstructure characteristic of a high-energy mechanosynthesis process was observed in all samples. As an example, Fig. 6a shows an SEM micrograph corresponding to the **BCZT-06** sample, which consists of large agglomerates formed from very small particles. After heating these powder samples at 900 °C/1 h, a very similar morphology was found, although a slight increase in size can be observed (Fig. 6b–f) and the small particles are clearly visible with a grain size below 50 nm.

The morphology of all the sintered samples is presented in Fig. 7, where the SEM micrographs of the fracture surface were taken in back scattered mode to better observe the differences in composition. The micrographs show a very small amount of close porosity, indicating a highly dense microstructure, especially for the **HP-BCZT** samples (Table 4). The average grain size is shown in each SEM image and also in Table 4. It is worth noting that despite the high temperature of 1400–1450 ºC used in both sintering procedures, a fine-grained microstructure was obtained. It has already been shown that high-energy mechanochemistry can produce powders with higher sintering activity, allowing high densification to be achieved without sintering additives, even in systems that require them [25]. For the **CS-BCZT** samples, grain size increases very slightly with the *x* value, from 1.12 to 1.52 μm. The largest average particle size was observed for the **HP-BCZT-06** sample (1.76 μm), decreasing to 1.29 μm for **HP-BCZT-055** and remaining around one μm for the other **HP** samples. The cumulative frequency (%) as a function of grain size (μm) of each sintered **BCZT** sample is displayed in Fig. 8. The same trend can be observed in the **CS** and **HP** curves, with a large slope below 1.5 μm indicating a small dispersion in the grain size values, founding a very small percentage of crystals with a size above 2 μm.

In the SEM micrographs in Fig. 7, some small areas of much darker contrast were observed, mostly around the residual porosity, and were

Table 3
Average chemical composition results obtained in different areas by EDS semiquantitative analysis in the SEM microscope.

Sample	Different areas	Ba (at%)	Ca (at%)	Zr (at%)	Ti (at%)
CS-BCZT−04	General (theoretical)	43.75 (44.00)	6.04 (6.00)	4.41 (6.00)	45.79 (44.00)
	BCZT	**43.75**	**6.04**	**4.41**	**45.79**
	Darker contrast phase	-	-	-	-
HP-BCZT−04	General (theoretical)	44.16 (44.00)	6.28 (6.00)	4.25 (6.00)	45.31 (44.00)
	BCZT	**44.37**	**6.06**	**4.06**	**45.51**
	Darker contrast phase	29.80	25.46	0.83	43.92
CS-BCZT−045	General (theoretical)	43.57 (43.25)	7.43 (6.75)	3.80 (5.50)	45.20 (44.50)
	BCZT	**43.33**	**7.78**	**3.25**	**45.63**
	Darker contrast phase	*34.58*	*17.19*	*2.65*	*45.59*
HP-BCZT−045	General (theoretical)	43.60 (43.25)	8.32 (6.75)	4.73 (5.50)	43.36 (44.50)
	BCZT	**44.25**	**6.70**	**4.02**	**45.03**
	Darker contrast phase	27.85	24.38	1.13	46.64
CS-BCZT−05	General (theoretical)	42.27 (42.50)	7.31 (7.50)	4.68 (5.00)	45.74 (45.00)
	BCZT	**42.93**	**6.67**	**4.30**	**46.17**
	Darker contrast phase	*31.75*	*18.14*	*2.59*	*47.53*
HP-BCZT−05	General (theoretical)	42.84 (42.50)	7.62 (7.50)	3.44 (5.00)	46.10 (45.00)
	BCZT	**42.81**	**7.17**	**3.49**	**46.53**
	Darker contrast phase	24.67	29.75	0.18	45.40
CS-BCZT−055	General (theoretical)	42.03 (41.75)	8.24 (8.25)	3.87 (4.50)	45.86 (45.50)
	BCZT	**42.00**	**8.09**	**3.34**	**46.68**
	Darker contrast phase	*31.53*	*19.85*	*2.23*	*46.39*
HP-BCZT−055	General (theoretical)	41.65 (41.75)	8.14 (8.25)	3.91 (4.50)	46.30 (45.50)
	BCZT	**42.16**	**5.95**	**6.18**	**45.72**
	Darker contrast phase	18.16	32.05	0.74	49.05
CS-BCZT−06	General (theoretical)	40.99 (41.00)	8.93 (9.00)	3.54 (4.00)	46.54 (46.00)
	BCZT	**41.83**	**9.10**	**2.45**	**46.62**
	Darker contrast phase	*26.31*	*23.35*	*1.85*	*48.49*
HP-BCZT−06	General (theoretical)	41.01 (41.00)	8.71 (9.00)	3.62 (4.00)	46.65 (46.00)
	BCZT	**42.03**	**8.35**	**3.48**	**46.13**
	Darker contrast phase	37.07	15.70	1.40	45.84

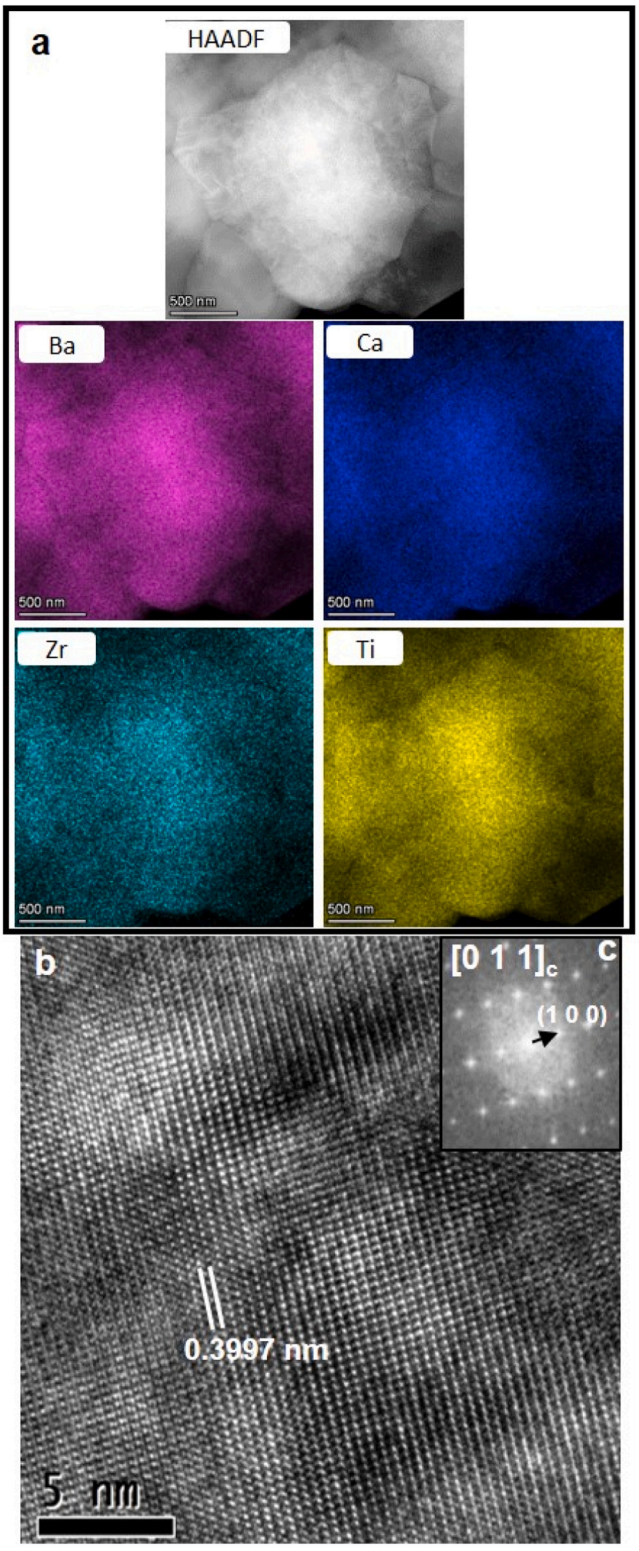

Fig. 9. HAADF/EDS, HRTEM and FFT results of the **CS-BCZT-04** sample, (a) HAADF image and elemental mapping of the same region, (b and c) HRTEM micrograph along the $[0\ 1\ 1]_c$ zone axis and the corresponding FFT.

determined by EDS to have a composition characterized mainly by a richer Ca content compared to the BCZT stoichiometry. These zones were associated with the secondary phases $A_4B_3O_{10}$ and A_2BO_4, in agreement with the XRD results. However, in some sintered samples, the extension of the darker contrast areas could not be explained by a secondary phase content of only about 3 % (or less) as determined by XRD. In these cases, the darker contrast could be associated with a different chemical composition of the cations in the BCZT phase, while maintaining the same perovskite structure.

The average chemical composition of BCZT and secondary phases was determined by semiquantitative EDS analysis performed on several small localized areas and the values obtained were compared with the overall composition obtained on much larger areas. The results are summarized in Table 3. In general, similar Ba and Ca contents were observed in the darker contrast areas, which were also poorer in Zr compared to the BCZT stoichiometry. At this point, it should be noted that for all samples and compositions the Ba atomic percentage was underestimated, while that of Ti was overestimated, due to the fact that the lines of both elements overlap in the energy emission spectrum, however, the presented results were corrected using a barium titanate as a standard for the Ba/Ti ratio measurement.

The microcharacterization of the sintered crystals from a structural and compositional point of view was carried out using ESTEM/EDS, ED and HRTEM techniques and representative results are presented for **CS-BCZT-04** (Fig. 9) and **HP-BCZT-055** samples (Fig. 10). Several areas of **CS-BCZT-04** sample were analyzed using HAADF/EDS and the results obtained indicate that the four constituent elements (Ba, Ca, Zr and Ti) of the BCZT phase are homogeneously distributed; as an example, the HAADF image of a crystal and the corresponding elemental mappings of Ba, Ca, Zr and Ti are presented (Fig. 9a). The HRTEM/ED study showed quite ordered crystals, all the micrographs, and their corresponding FFTs along different zone axis could be indexed to cubic symmetry, space group *Pm-3 m* (121) and cell parameter equal to 0.399 nm. Fig. 9b, c show a HR image and the corresponding FFT taken along the [0 1 1]c zone axis, the (1 0 0) spacing is marked on the image and FFT.

The study of **HP-BCZT-055** sample by HAADF/EDS is shown in Fig. 10a and b. Most of the analyzed areas exhibited Ba, Ca, Zr and Ti elemental mappings with homogeneous composition (Fig. 10a), however, some areas were also observed where the amount of Ca is greater (Fig. 10b). This result is in agreement with that obtained by SEM/EDS for the same sample. From the HRTEM analysis, it was understood that this sample is composed of many crystals with cubic symmetry like **CS-BCZT-04** sample. However, a few crystals with non-cubic microdomains were found, as an example shown in Fig. 10c. This crystal was indexed in a tetragonal system, *P4mm* (99) space group, and oriented along the $[0\ 1\ 0]_t$ zone axis (FFT in Fig. 10d). It exhibits very well-ordered features and cell parameters of a=0.4064 nm and c=0.4127 nm were measured.

Table 4 shows the piezoelectric coefficient (d_{33}) of the sintered samples. Despite the pseudocubic symmetry, both **CS-BCZT** and **HP-BCZT** ceramic samples exhibited a piezoelectric response. López-Blanco et al. [17] have suggested that other mechanisms different to the asymmetry of the structure, such as electric-field-induced phase transformation, should be considered to explain the piezoelectric response in this type of pseudocubic structures. Kuhfuß et al. [26] have studied this effect by varying the grain size and have demonstrated significant structural changes upon application of an electric field to polycrystalline $Ba_{0.85}Ca_{0.15}Zr_{0.1}Ti_{0.9}O_3$.

Due to the small grain size (< 2 μm), the d_{33} values were always below 100 pC/N. The strong influence of grain size on the properties of these solid solutions, as previously mentioned, is well known. The domain size and 90º domain walls motion are directly related to the grain size in these perovskite-structured ceramics when the grain size is below 10 μm [12]. Because fine-grained- BCZT results in smaller domains and inhibits domain wall motion during polarization, these materials exhibit lower d_{33} values than coarse-grained ones [12,27]. The increase in non-ferroelectric grain boundaries and inner stresses in these fine-grained BCZTs also causes a decrease in permittivity (ε') [4,27]. Yan et al. [5] have reported a critical grain size of ~12.9 μm for the same composition of BCZT-06, which maximizes ε' and stabilizes d_{33}. In addition to the constriction of wall motion, the small grain size leads to a decrease in the lattice aspect ratio (c/a), with a consequent loss of the

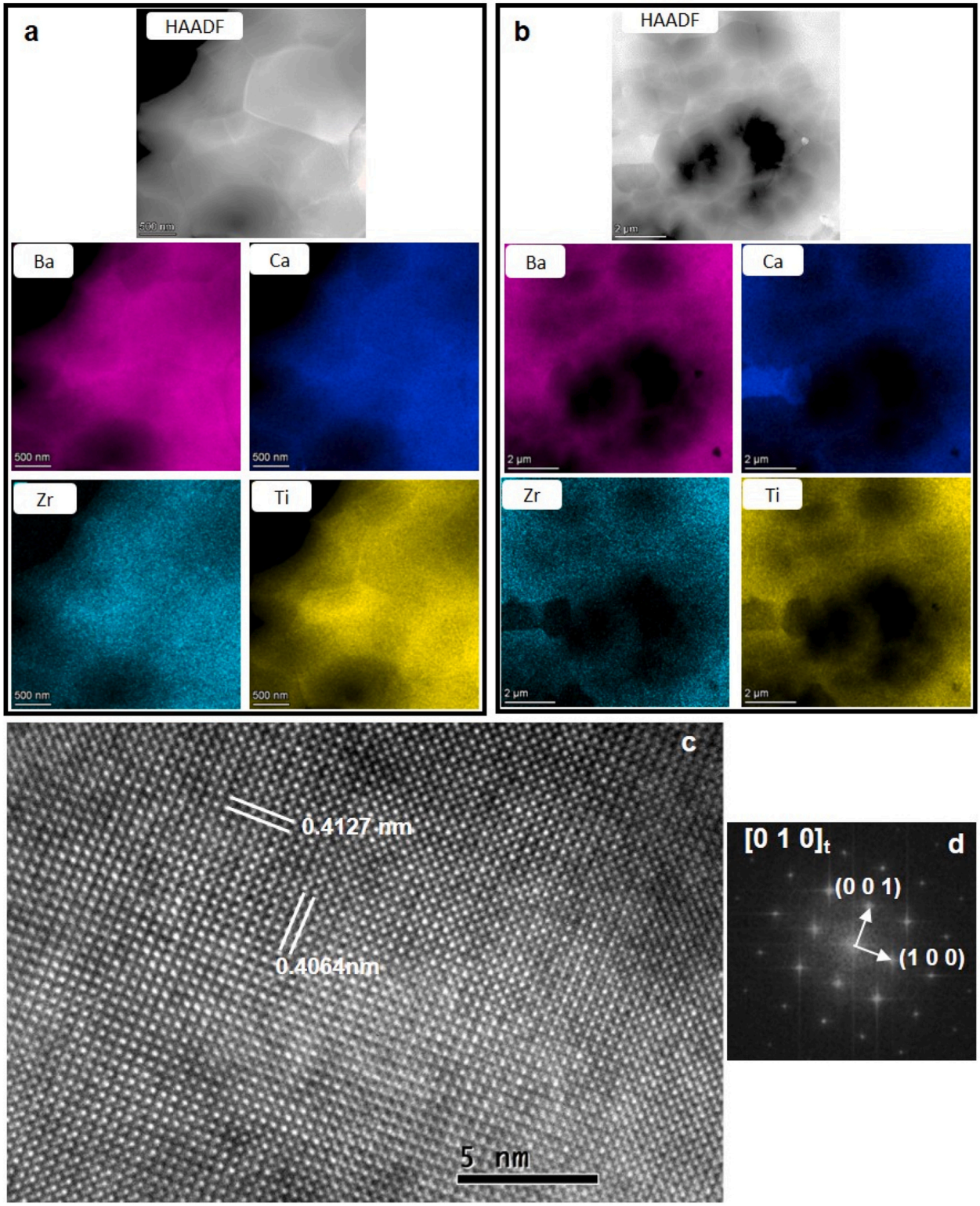

Fig. 10. HAADF/EDS, HRTEM and FFT results of the **HP-BCZT-055** sample, (a and b) HAADF image and elemental mappings of two different regions, (c and d) HRTEM micrograph along the $[0\ 1\ 0]_t$ zone axis and the corresponding FFT.

ferroelectric properties at a critical submicrometric grain size [26].

Since HP prevented the segregation of secondary phases and increased the relative density, a significant increase in d_{33} was obtained for all HP-BCZT, compared to the CS-BCZT of the same stoichiometry. These results are in agreement with those published by Ye et al. [28] for coarse-grained BCZT. In addition, although the XRD results for **CS-BCZT** and **HP-BCZT** samples mostly showed pseudocubic symmetry, when analyzing the Williamson-Hall plot for these samples (Fig. 11), which shows the dependence of the XRD line broadening as a function of the 2θ angle, the typical linear behavior for a single phase was observed only for **CS-BCZT** samples. However, a deviation from linearity with scattered data was clearly observed for **HP-BCZT** samples. This artifact of

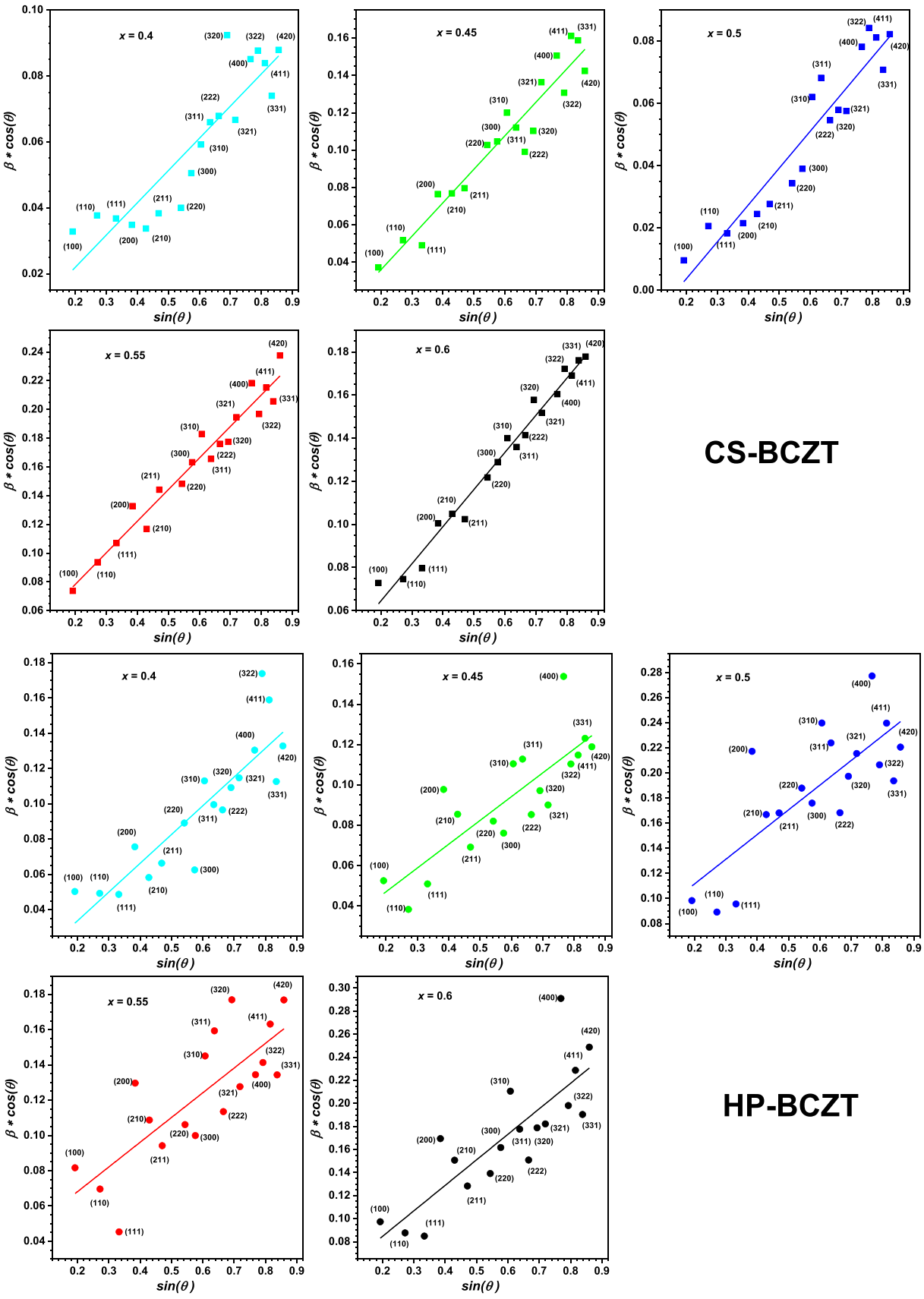

Fig. 11. Williamson-Hall plot for **CS-BCZT** and **HP-BCZT** ceramic samples. β is the integral breadth of XRD peaks.

Table 4
Influence of the stoichiometry and sintering process on the piezoelectric coefficient of BCZT samples.

Sample	*Relative density* (%)	*Average grain size* (s.d.) (μm)	d_{33} (pC/N)	d_{33} (24 h) (pC/N)	ε'
CS-BCZT−04	97.4	1.12 (0.76)	5.1	-	2210
CS-BCZT−045	96.6	1.19 (0.85)	11.0	9.2	2210
CS-BCZT−05	98.8	1.20 (0.60)	9.8	7.8	2220
CS-BCZT−055	98.3	1.35 (0.79)	16.6	16.6	3890
CS-BCZT−06	97.5	1.52 (1.2)	21.0	20.0	3360
HP-BCZT−04	99.2	0.96 (0.35)	10.0	6.5	2450
HP-BCZT−045	99.8	1.01 (0.82)	20.5	16.1	3220
HP-BCZT−05	99.9	0.96 (0.64)	30.0	20.0	4380
HP-BCZT−055	99.7	1.29 (0.44)	60.0	47.0	3830
HP-BCZT−06	99.8	1.76 (1.5)	88.0	80.6	3280

Table 5
Piezoelectric and dielectric permittivity of BCZT in previously published works.

Solid solution	Synthesis method (sintering process)	Grain size (μm)	ε'	d_{33} (pC/N)	Ref.
$Ba_{0.85}Ca_{0.15}Zr_{0.1}Ti_{0.9}O_3$	Solid-State	0.4	~3000	~72	[12]
	(Spark plasma sintering)	1.5	<3000	<200	
$Ba_{0.85}Ca_{0.15}Zr_{0.1}Ti_{0.9}O_3$	Mechanochemistry	0.90 ± 0.38	-	-	[17]
	(Flash sintering)	1.88 ± 0.98	7470	145	
		2.15 ±0.91	5500	105	
		2.23 ± 0.90	3290	100	
$Ba_{0.85}Ca_{0.15}Zr_{0.1}Ti_{0.9}O_3$	Solid-state	2.48	<1250	-	[29]
	(Conventional sintering)				
$Ba_{0.85}Ca_{0.15}Zr_{0.1}Ti_{0.9}O_3$	Mechanochemistry	1.0	<2000	17 ± 2	[16]
	(Spark plasma sintering)	2.0	<2500	45 ± 2	
$Ba_{0.85}Ca_{0.15}Zr_{0.1}Ti_{0.9}O_3$	Mechanochemistry	4.7	-	270	[6]
	(Conventional Sintering)				
$Ba_{0.85}Ca_{0.15}Zr_{0.1}Ti_{0.9}O_3$	Sol-gel	1.5	-	39	[4]
	(Conventional Sintering)				
$Ba_{0.85}Ca_{0.15}Zr_{0.1}Ti_{0.9}O_3$	Sol-gel	0.5	736	21	[27]
	(Conventional sintering)				
$Ba_{0.85}Ca_{0.15}Zr_{0.1}Ti_{0.9}O_3$	Mechanosynthesis	0.96 ± 0.11	4380	30	This work
	(HP sintering)				
$0.4Ba(Zr_{0.2}Ti_{0.8})O_3-0.6(Ba_{0.7}Ca_{0.3})TiO_3$	Solid State	2	-	120	[5]
	and high energy milling				
	(Two-step sintering)				
$0.4Ba(Zr_{0.2}Ti_{0.8})O_3-0.6(Ba_{0.7}Ca_{0.3})TiO_3$	Mechanosynthesis	1.76 ± 0.04	3280	88	This work
	(HP sintering)				

anisotropic line broadening suggests the presence of very close or overlapping diffraction lines due to different crystal structures, which is consistent with the tetragonal microdomains observed by TEM in these samples and can also explain the higher d_{33} values found. Additionally, the use of lower sintering temperatures in HP could lead to higher d_{33} values because of a lower concentration of point defects acting as pinning points for domain wall motion [17].

Table 4 shows how d_{33} increases with decreasing Ba and Zr stoichiometry, as expected [23], and the maximum d_{33} value was obtained for **HP-BCZT-06,** reaching a value of 88.0 pC/N. This value is higher than most previously reported for BZCT solid solutions of comparable average grain size, typically $Ba_{0.85}Ca_{0.15}Zr_{0.1}Ti_{0.9}O_3$ (Table 5).

4. Conclusions

All studied stoichiometries of the BCZT solid-solution were successfully formed by high-energy mechanochemical synthesis after 120 min, showing a pseudocubic perovskite phase with homogeneously distributed A- and B-cations in the crystal structure. The residual $BaCO_3$ impurity phase in the as-milled samples, derived from the BaO_2 precursor, disappeared after annealing at 900 ºC. After sintering, the BCZT perovskite phases exhibited a crystal structure more compatible with pseudocubic symmetry and a fine-grained microstructure with an average grain size <1.8 μm in all cases. Conventional sintered samples with high x values showed the presence of a non-negligible amount of a secondary phase with chemical formula $A_4B_3O_{10}$ and Ruddlesden-Popper structure. Nevertheless, HP prevented this secondary phase segregation and increased the relative density. Williamson-Hall plot showed the typical linear behavior for **CS-BCZT** samples, but a deviation from linearity with scattered data was clearly observed for **HP-BCZT** samples, suggesting the presence of different crystal structures, which was consistent with the tetragonal microdomains observed by TEM.

Despite the pseudocubic symmetry, both **CS-BCZT** and **HP-BCZT** ceramic samples exhibited d_{33} values ranging from 5.1 to 21 pC/N and from 10.0 to 88.0 pC/N, respectively. Due to the strong influence of the fine-grain size on the properties of these solid-solutions, the d_{33} values were less than 100 pC/N, but higher than most previously reported values. Electric-field-induced phase transformation should be considered as responsible for the piezoelectric response in this type of pseudocubic structures. The presence of different crystal structures, supported by the Williamson-Hall plot and TEM analysis, as well as the higher density and lower sintering temperature in HP samples could be responsible for the increase in d_{33} values compared to those of CS samples.

Declaration of Competing Interest

The authors declare that they have no known competing financial interests or personal relationships that could have appeared to influence the work reported in this paper.

Data availability

Data will be made available on request.

Acknowledgements

The authors acknowledge the grant TED2021–131458A-I00 funded by MICIU/AEI/ 10.13039/501100011033 and by the "European Union NextGenerationEU/PRTR"; and the grant PID2020–117648RB-I00 funded by MICIU/AEI/10.13039/501100011033.

References

[1] Q.M. Zhang, J. Zhao, Electromechanical properties of lead zirconate titanate piezoceramics under the influence of mechanical stresses, 1518, Ieee Trans. Ultrason., Ferroelectr., Freq. Control 46 (1999) 1518–1526.
[2] W. Liu, X. Ren, Large piezoelectric effect in Pb-free ceramics, Phys. Rev. Lett. 103 (2009), https://doi.org/10.1103/PhysRevLett.103.257602.
[3] A. Reyes-Montero, F. Rubio-Marcos, L. Pardo, A. Del Campo, R. López-Juárez, M. E. Villafuerte-Castrejón, Electric field effect on the microstructure and properties of $Ba_{0.9}Ca_{0.1}Ti_{0.9}Zr_{0.1}O_3$ (BCTZ) lead-free ceramics, J. Mater. Chem. A Mater. 6 (2018) 5419–5429, https://doi.org/10.1039/c7ta09798k.
[4] I. Coondoo, N. Panwar, D. Alikin, I. Bdikin, S.S. Islam, A. Turygin, V.Y. Shur, A. L. Kholkin, A comparative study of structural and electrical properties in lead-free BCZT ceramics: Influence of the synthesis method, Acta Mater. 155 (2018) 331–342, https://doi.org/10.1016/j.actamat.2018.05.029.
[5] X. Yan, M. Zheng, Y. He, M. Zhu, Y. Hou, Origin of superior dielectric and piezoelectric properties in $0.4Ba(Zr_{0.2}Ti_{0.8})O_3$–$0.6(Ba_{0.7}Ca_{0.3})TiO_3$ at intermediate grain sizes, J. Eur. Ceram. Soc. 40 (2020) 3936–3945, https://doi.org/10.1016/j.jeurceramsoc.2020.03.071.
[6] H. Amorín, M. Venet, E. Chinarro, P. Ramos, M. Algueró, A. Castro, Lead-free $Ba_{0.85}Ca_{0.15}Zr_{0.1}Ti_{0.9}O_3$ ferroelectric ceramics with refined microstructure and high strain under electric field by mechanosynthesis, J. Eur. Ceram. Soc. 42 (2022) 4907–4916, https://doi.org/10.1016/j.jeurceramsoc.2022.04.061.
[7] W. Liu, L. Cheng, S. Li, Prospective of $(BaCa)(ZrTi)O_3$ lead-free piezoelectric ceramics, Cryst. (Basel) 9 (2019), https://doi.org/10.3390/cryst9030179.
[8] J. Gao, X. Hu, L. Zhang, F. Li, L. Zhang, Y. Wang, Y. Hao, L. Zhong, X. Ren, Major contributor to the large piezoelectric response in (1 -x)$Ba(Zr_{0.2}Ti_{0.8})O_3$-x $(Ba_{0.7}Ca_{0.3})TiO_3$ ceramics: domain wall motion, Appl. Phys. Lett. 104 (2014), https://doi.org/10.1063/1.4885675.
[9] T. Zheng, J. Wu, D. Xiao, J. Zhu, Recent development in lead-free perovskite piezoelectric bulk materials, Prog. Mater. Sci. 98 (2018) 552–624, https://doi.org/10.1016/j.pmatsci.2018.06.002.
[10] L. Zhang, L. Zhao, L. He, D. Wang, Y. Sun, D. Wang, X. Lou, L. Zhang, M. A. Carpenter, New degree of freedom in determining superior piezoelectricity at the lead-free morphotropic phase boundary: the invisible ferroelectric crossover, ACS Appl. Mater. Interfaces 14 (2022) 1434–1442, https://doi.org/10.1021/acsami.1c19856.
[11] N. Pisitpipathsin, P. Kantha, K. Pengpat, G. Rujijanagul, Influence of Ca substitution on microstructure and electrical properties of $Ba(Zr,Ti)O_3$ ceramics, : Ceram. Int (2013), https://doi.org/10.1016/j.ceramint.2012.10.031.
[12] J. Hao, W. Bai, W. Li, J. Zhai, Correlation between the microstructure and electrical properties in high-performance $(Ba_{0.85}Ca_{0.15})(Zr_{0.1}Ti_{0.9})O_3$ lead-free piezoelectric ceramics, J. Am. Ceram. Soc. 95 (2012) 1998–2006, https://doi.org/10.1111/j.1551-2916.2012.05146.x.
[13] F. Benabdallah, C. Elissalde, U.C.C. Seu, D. Michau, A. Poulon-Quintin, M. Gayot, P. Garreta, H. Khemakhem, M. Maglione, Structure-microstructure-property relationships in lead-free BCTZ piezoceramics processed by conventional sintering and spark plasma sintering, J. Eur. Ceram. Soc. 35 (2015) 4153–4161, https://doi.org/10.1016/j.jeurceramsoc.2015.06.030.
[14] C.E. Ciomaga, L.P. Curecheriu, V.A. Lukacs, N. Horchidan, F. Doroftei, R. Valois, M. Lheureux, M.H. Chambrier, L. Mitoseriu, Optimization of processing steps for superior functional properties of (Ba, Ca)(Zr, Ti)O_3 Ceramics, Materials 15 (2022), https://doi.org/10.3390/ma15248809.
[15] A.C. Hernández-Moreno, A. Reyes-Montero, B. Carreño-Jiménez, M. Acuautla, L. Pardo, Ferroelectric, dielectric and electromechanical performance of $Ba_{0.92}Ca_{0.08}Ti_{0.95}Zr_{0.05}O_3$ ceramics with an enhanced curie temperature, Materials 16 (2023), https://doi.org/10.3390/ma16062268.
[16] H. Amorín, M. Venet, J.E. García, D.A. Ochoa, P. Ramos, J. López-Sánchez, J. Rubio-Zuazo, A. Castro, M. Algueró, Insights into the early size effects of lead-free piezoelectric $Ba_{0.85}Ca_{0.15}Zr_{0.1}Ti_{0.9}O_3$, Adv. Electron Mater. 10 (2024), https://doi.org/10.1002/aelm.202300556.
[17] S. López-Blanco, D.A. Ochoa, H. Amorín, A. Castro, M. Algueró, J.E. García, Fine-grained high-performance $Ba_{0.85}Ca_{0.15}Zr_{0.1}Ti_{0.9}O_3$ piezoceramics obtained by current-controlled flash sintering of nanopowders, J. Eur. Ceram. Soc. 43 (2023) 7440–7445, https://doi.org/10.1016/j.jeurceramsoc.2023.08.012.
[18] M. Mureddu, J.F. Bartolomé, S. Lopez-Esteban, M. Dore, S. Enzo, Á. García, S. Garroni, L. Pardo, Solid state processing of BCZT piezoceramics using ultra low synthesis and sintering temperatures, Materials 16 (2023), https://doi.org/10.3390/ma16030945.
[19] F.J. Garcia-Garcia, M.J. Sayagués, F.J. Gotor, A novel, simple and highly efficient route to obtain $PrBaMn_2O_{5+\delta}$ double perovskite: mechanochemical synthesis, Nanomaterials 11 (2021) 1–18, https://doi.org/10.3390/nano11020380.
[20] F.J. Garcia-Garcia, Y. Tang, F.J. Gotor, M.J. Sayagués, Development by mechanochemistry of $La_{0.8}Sr_{0.2}Ga_{0.8}Mg_{0.2}O_{2.8}$ electrolyte for SOFCs, Materials 13 (2020), https://doi.org/10.3390/ma13061366.
[21] M.J. Sayagués, F.J. Gotor, M. Pueyo, R. Poyato, F.J. Garcia-Garcia, Mechanosynthesis of $Sr_{1-x}La_xTiO_3$ anodes for SOFCs: structure and electrical conductivity, J. Alloy. Compd. 763 (2018) 679–686, https://doi.org/10.1016/j.jallcom.2018.05.243.
[22] R. Moriche, D. Marrero-López, F.J. Gotor, M.J. Sayagués, Chemical and electrical properties of LSM cathodes prepared by mechanosynthesis, J. Power Sources 252 (2014) 43–50, https://doi.org/10.1016/j.jpowsour.2013.11.093.
[23] D.K. Dobesh, A. Gadelmawla, H. Miyazaki, M. Hinterstein, K. Kimura, J.G. Maier, S. Banerjee, O. Zeair, S.C. Mehta, L.L. da Silva, N.H. Khansur, K. Hayashi, D. de Ligny, K.G. Webber, M.R. Cicconi, The role of Ca/Zr ratio on the local structure and phase transitions in lead-free $(Ba,Ca)(Zr,Ti)O_3$, J. Eur. Ceram. Soc. (2024), https://doi.org/10.1016/j.jeurceramsoc.2024.03.003.
[24] D. Wang, Z. Jiang, B. Yang, S. Zhang, M. Zhang, F. Guo, W. Cao, Phase diagram and enhanced piezoelectric response of lead-free $BaTiO_3$ – $CaTiO_3$ – $BaHfO_3$ system, J. Am. Ceram. Soc. 97 (2014) 3244–3251, https://doi.org/10.1111/jace.13137.
[25] L. Chao, Y. Hou, M. Zheng, Y. Yue, M. Zhu, $NaNbO_3$ nanoparticles: Rapid mechanochemical synthesis and high densification behavior, J. Alloy. Compd. 695 (2017) 3331–3338, https://doi.org/10.1016/j.jallcom.2016.12.036.
[26] M. Kuhfuß, J.G. Maier, D.A. Hall, B. Xie, A.K. Kleppe, A. Martin, K.I. Kakimoto, N. H. Khansur, K.G. Webber, In situ electric field-dependent structural changes in (Ba, Ca)(Zr,Ti)O_3 with varying grain size, J. Appl. Phys. 135 (2024), https://doi.org/10.1063/5.0203652.
[27] P. Bharathi, K.B.R. Varma, Grain and the concomitant ferroelectric domain size dependent physical properties of $Ba_{0.85}Ca_{0.15}Zr_{0.1}Ti_{0.9}O_3$ ceramics fabricated using powders derived from oxalate precursor route, J. Appl. Phys. 116 (2014), https://doi.org/10.1063/1.4900494.
[28] S. Ye, J. Fuh, L. Lu, Y.L. Chang, J.R. Yang, Structure and properties of hot-pressed lead-free $(Ba_{0.85}Ca_{0.15})(Zr_{0.1}Ti_{0.9})O_3$ piezoelectric ceramics, RSC Adv. 3 (2013) 20693–20698, https://doi.org/10.1039/c3ra43429j.
[29] X. Zhang, G. Chen, Z. Liu, M. Yu, C.M. Leung, C. Wang, D. Chen, M. Zeng, Achieved excellent energy storage properties and ultrahigh power density of $Ba_{0.85}Ca_{0.15}Zr_{0.1}Ti_{0.9}O_3$ lead-free ceramics modified by $Bi(Mg_{0.5}Hf_{0.5})O_3$, J. Alloy. Compd. 968 (2023), https://doi.org/10.1016/j.jallcom.2023.172171.